

Preparation of Folic Acid-conjugated Albumin Nanoparticles Containing Paclitaxel using High-pressure Homogenisation Coagulation Method

Yan Chu

Qiqihar Medical College: Qiqihar Medical University

Shuo Chai

Qiqihar Medical College: Qiqihar Medical University

Hong Pan

Qiqihar Medical College: Qiqihar Medical University

Jiayi Qian

Qiqihar Medical College: Qiqihar Medical University

Cuiyan Han

Qiqihar Medical College: Qiqihar Medical University

Xiaoyu Sui (✉ suixiaoyu@outlook.com)

Qiqihar Medical University <https://orcid.org/0000-0001-8741-2902>

Tingting Liu

Qiqihar Medical College: Qiqihar Medical University

Nano Express

Keywords: Albumin nanoparticles, Paclitaxel, Folic acid, High pressure homogenization, Cell uptake

Posted Date: March 9th, 2021

DOI: <https://doi.org/10.21203/rs.3.rs-221888/v1>

License: © ⓘ This work is licensed under a Creative Commons Attribution 4.0 International License.

[Read Full License](#)

1 Preparation of folic acid-conjugated albumin nanoparticles
2 containing paclitaxel using high-pressure homogenisation
3 coagulation method

4 Yan Chu, Shuo Chai, Hong Pan, Jiayi Qian, Cuiyan Han, Xiaoyu Sui *, Tingting Liu *

5 College of Pharmacy, Qiqihar Medical University, Qiqihar 161006, China

6

7 *Corresponding authors: Xiaoyu Sui, Tingting Liu, email: suixiaoyu@outlook.com

8 (Xiaoyu Sui) and ltting@outlook.com (Tingting Liu).

9 **Abstract**

10 In this study, we prepared and evaluated folic acid-conjugated albumin-paclitaxel
11 (FA-BSA-PTX) nanoparticles using a new green technique, called the high-pressure
12 homogenisation coagulation method (HPHCM). The effect of process parameters
13 such as BSA concentration, coagulant concentration, homogenisation time,
14 homogenisation pressure, water/ethanol ratio, and BSA/PTX ratio was analysed to
15 optimise nanoparticle size, albumin conversion rate, and encapsulation efficiency. BSA
16 concentration was found to exert a great influence on albumin conversion rate and
17 particle size. Meanwhile, the BSA/PTX ratio significantly affected the nanoparticle
18 encapsulation efficiency. Electron microscopy showed that the freeze-dried particles
19 mostly existed in the form of dimers and trimers with an average particle size of 300–
20 400 nm. Infrared spectroscopy indicated that PTX was well encapsulated in BSA.
21 Raman spectra of the synthesised nanoparticles indicated changes in the disulphide
22 bond configuration and protein structure. In vitro drug-release analysis showed that
23 crosslinked nanoparticles exhibited a sustained release. Furthermore, in vitro cell-
24 uptake studies on HeLa cells showed that FA can be used as a targeting ligand for
25 albumin carriers to enhance the active targeting effect of the nanoparticles with a high
26 FR expression. These results suggest that HPHCM is an effective method to prepare
27 FA-BSA-PTX drug-delivery systems.

28 **Keywords:** Albumin nanoparticles; Paclitaxel; Folic acid; High pressure
29 homogenization; Cell uptake

30 1. Introduction

31 Nanoparticle-based drug-delivery systems are considered to show great potential
32 for cancer treatment as these carrier systems exhibit high drug absorption, adjustable
33 drug-release rate, and targeted delivery, especially in the case of hydrophobic drugs
34 [1,2]. Previous reports have suggested that nanoparticles hundreds of nanometers in
35 diameter can passively reach tumors by virtue of the enhanced permeability and
36 retention (EPR) effect [3]. Lately, nanoparticle drug-delivery systems with albumin as
37 a carrier are receiving much attention. As an endogenous substance, albumin plays a
38 unique role in reducing the phagocytosis of nanoparticles, thus prolonging the in vivo
39 circulation of drugs [4,5]. In addition, albumin is a macromolecular carrier, whose pores
40 can encapsulate hydrophobic compounds. Moreover, albumin can be tightly but
41 reversibly bound to certain drugs through non-covalent bonds to realize drug transport
42 in vivo and their release at the target cell surface [6]. Bovine serum albumin (BSA) is
43 one of the most commonly used drug carrier proteins owing to its good biocompatibility,
44 low cost, and easy purification [7]. BSA-based nanoparticle drug-delivery systems
45 exhibit various functions and binding properties such as good stability and a high
46 binding capacity for drugs with different physical and chemical properties. In addition,
47 the BSA molecule contains functional groups such as amino and carboxyl groups
48 owing to which albumin nanoparticle carrier surfaces can be easily modified by ligands
49 [8,9].

50 The main purpose of targeted cancer therapy is to deliver drugs to tumour cells in
51 order to localise high drug concentrations at tumour sites and reduce side effects
52 [10,11]. Passive targeting is inherent in drug-loaded nanoparticles. Meanwhile, to
53 achieve an active targeting function, ligand modification may be adopted [12]. Folic
54 acid (FA), a common targeting ligand, is a low molecular weight vitamin whose folate
55 receptor (FR) is overexpressed on the surfaces of a variety of cancer cells such as
56 breast, ovary, lung, kidney, colon, and brain cancer cells; however, its expression is
57 minimal in healthy tissues and organs. The FR expression level in cancer cells is 100–

58 300 times higher than that in normal tissues [13]. Therefore, targeted delivery can be
59 achieved by FA-linked nanoparticles entering the cytoplasm via FR mediation and
60 endocytosis. FR is extensively studied for cancer diagnosis and treatment [14] due to
61 several key characteristics. Firstly, FA can be easily synthesised, is inexpensive, and
62 is easy to chemically modify and characterise [15]. Secondly, FA itself has no
63 immunogenicity and exhibits high structural stability even after chemical modification,
64 thus maintaining a high affinity with FR [16].

65 Traditionally, albumin nanoparticles are prepared by chemical crosslinking, thermal
66 denaturation, or desolvation. Chemical crosslinking is non-specific and depends only
67 on the reactivity of the nucleophilic groups (such as amino and hydroxyl groups) in the
68 protein structure. Nevertheless, the crosslinking agents used in this method, such as
69 formaldehyde, exhibit high levels of toxicity and result in residues [17,18]. Thermal
70 denaturation, by techniques such as solution thermal crosslinking or spray drying,
71 irreversibly alters the protein structure and the resultant protein nanoparticles exhibit
72 poor biodegradability and a wide size distribution [19]. Using the desolvation method,
73 nanoparticles are obtained by continuously dropping a water-miscible organic phase,
74 such as ethanol, into an aqueous albumin solution under continuous stirring until the
75 solution becomes turbid [20]. The formed nanoparticles are morphologically unstable
76 and require hardening by crosslinking with glutaraldehyde. During this process,
77 however, bioactive macromolecules may be deactivated and residues of harmful
78 solvents may be formed. Toxic solvents, such as acetone, chloroform, and
79 dichloromethane are required in the methods described here, which may lead to
80 adverse health effects [21].

81 Green chemistry is a powerful ally of the pharmaceutical industry [22]. To
82 synthesise nanoparticles in a 'green' manner, a non-toxic solvent medium should be
83 used; in addition, non-toxic materials should be used to stabilise these nanoparticles
84 [23]. Most of the preparation methods reported thus far rely heavily on organic solvents,
85 which leads to toxicity. To counter this problem, environmentally friendly and
86 sustainable green strategies methods are also being developed to prepare

87 nanoparticles [24,25].

88 In this study, we used a new green technique, called the high-pressure
89 homogenisation coagulation method (HPHCM), to prepare albumin nanoparticles. In
90 a water-based system, albumin nanoparticles were formed using a coagulant;
91 simultaneously, superoxide dismutase, produced by high-pressure homogeneous
92 cavitation, was used to promote the formation of disulphide bonds between the
93 cysteine residues of protein molecules. FA-BSA-paclitaxel (PTX) nanoparticles
94 targeting FR were prepared with PTX as the model drug. The size and entrapment
95 efficiency of the nanoparticles were analysed along with their physical and chemical
96 properties. The in vitro release characteristics of nanoparticles obtained by secondary
97 curing with different crosslinking agents were compared. The uptake of FA-BSA-PTX
98 into HeLa cells was evaluated using laser confocal microscopy (LCSM).

99 **2. Materials and methods**

100 2.1. Materials

101 PTX, calcium lactate, and gluconolactone were procured from Dalian Meilun
102 Biology Technology Co., Ltd. (Dalian, China). BSA, calcium chloride, and magnesium
103 chloride were purchased from Sigma Aldrich Co. Ltd. (Shanghai, China), and methanol
104 was purchased from J&K Scientific Ltd. (Beijing, China). N,N'-
105 Dicyclohexylcarbodiimide (DCC), FA, and N-hydroxysuccinimide (NHS) were obtained
106 from Yuan Ye Biotechnology Co. Ltd. (Shanghai, China); ethanol and dichloromethane
107 were purchased from Sinopharm Chemical Reagent Co. Ltd. (Beijing, China). Pure
108 water was prepared using a Milli-Q water purification system (Millipore, Bedford, MA,
109 USA).

110 2.2. Preparation of albumin nanoparticles

111 The schematic diagram of the experimental apparatus are shown in Fig. 1. An
112 albumin solution was prepared by dissolving 20 mg of the coagulant ($MgCl_2$) and 400
113 mg of BSA in 40 mL (50 °C) of pure water. Meanwhile, 40 mg of PTX was dissolved in
114 ethanol. The albumin solution was slowly added to the material cup of a high-pressure

115 homogeniser and the temperature of the circulating water bath was set at 50 °C. PTX
116 solution was added dropwise (1 mL/min) to this pre-heated albumin solution at a
117 pressure of 150 bar. Subsequently, the homogenisation pressure was adjusted to the
118 target value and after a set time period, drug-loaded albumin nanoparticle suspensions
119 could be obtained. These solutions were centrifuged at 8000 rpm for 8 min in an
120 ultracentrifuge (CP70MX, Hitachi Koki Co. Ltd., Japan) and the supernatant was
121 removed. Later, the obtained precipitates were lyophilised with cryoprotectant
122 mannitol (1:1 mass ratio). After pre-freezing for 12 h at - 80 °C, the nanoparticles was
123 freeze-dried at a shelf temperature of -50 °C for 24 h at a chamber pressure of 1–20
124 Pa in a lyophiliser (SJIA-10N, Ningbo Shuangjia Science Technology Development Co.
125 Ltd., China).

126 2.3. Preparation of crosslinked albumin nanoparticles

127 An albumin-nanoparticle suspension was prepared as described in paragraph 2.2,
128 centrifuged at 8000 rpm for 8 min using an ultracentrifuge (CP70MX, Hitachi Koki Co.
129 Ltd., Japan), and the supernatant was removed. Purified water (6 mL) was added to
130 the reaction flask to disperse the precipitate. Three crosslinking agents (genipin,
131 vanillin, and glutaraldehyde) were added to this dispersion and allowed to react for 90
132 min at 60 °C. Subsequently, the precipitates were lyophilised with cryoprotectant
133 mannitol (1:1 mass ratio). After prefreezing for 12 h at - 80 °C, freeze-drying was
134 carried out at a shelf temperature of -50 °C for 24 h at a chamber pressure of 1–20
135 Pa in a lyophiliser (SJIA-10N, Ningbo Shuangjia Science Technology Development Co.
136 Ltd., China).

137 2.4. Preparation of FA-BSA-PTX and FITC-BSA-PTX nanoparticles

138 FA-BSA-PTX nanoparticles were prepared through a reaction between FA-NHS
139 and BSA-PTX [26]. FA-NHS was synthesised as follows. Initially, 300 mg of FA was
140 dissolved in 6 mL of dimethyl sulphoxide (DMSO) and to this solution, 150 µL of
141 triethylamine, 282 mg of DCC, and 156 mg of NHS were added. The resultant mixture
142 was stirred overnight at room temperature (25 °C). The insoluble by-product,

143 dicyclohexylure (DCU), was removed using filtration, and FA-NHS was precipitated by
144 pouring the filtrate into an ice-cold solution of anhydrous ether containing 30% acetone.
145 After centrifuging the precipitate and washing it with anhydrous ether, it was subjected
146 to suction filtration and vacuum drying to yield FA-NHS.

147 A small quantity of FA-NHS (10 mg) was dissolved in 2 mL of an $\text{Na}_2\text{CO}_3/\text{NaHCO}_3$
148 buffer solution (0.2 M, pH 10); meanwhile, freeze-dried BSA-PTX nanoparticles were
149 also dissolved in the same buffer solution. The prepared FA-NHS solution was added
150 dropwise to the BSA-PTX solution and stirred gently for 2 h. At the end of this time
151 period, the FA-BSA-PTX solution was subjected to centrifugal ultrafiltration (50 kDa,
152 $3,214 \times g$, 10 min) and washed with deionised water. The obtained product was then
153 freeze-dried.

154 BSA was diluted in a $\text{Na}_2\text{CO}_3/\text{NaHCO}_3$ buffer solution (25 mM, pH 9.8) at a
155 concentration of 5 mg/mL. Subsequently, FITC was added to the BSA solution to yield
156 a final concentration of 0.1 mg/mL and the solution was incubated overnight at room
157 temperature. The final product was obtained by centrifuging the mixed solution in
158 ultrafiltration tubes with a molecular weight cut-off of 50 kDa at $12,857 \times g$ for 10 min.
159 The product was washed with the $\text{Na}_2\text{CO}_3/\text{NaHCO}_3$ buffer and centrifuged twice to
160 obtain FITC-BSA. FITC-BSA-PTX and FITC-FA-BSA-PTX were prepared using a
161 similar process.

162 2.5. Quantitative determination of PTX using high-performance liquid 163 chromatography (HPLC)

164 PTX content was analysed on a C18 HPLC column ($250 \times 4.6 \text{ mm}^2$, 5 μm ;
165 Shandong Lunan Ruihong Chemical Instrument Co. Ltd.) with methanol and water
166 (75:25 v/v) as mobile phase A and methanol (100%) as mobile phase B (100%) at a
167 flow rate of 1.0 mL/min. The analytes were evaluated using a wavelength detector at
168 227 nm. The injection volume was set at 20 μL . A linear regression equation, $Y =$
169 $0.6913X + 5.925$ ($R^2 = 0.9995$), where Y indicates peak area and X represents mass
170 concentration, was observed in the range of 10–100 $\mu\text{g/mL}$, illustrating a good linear

171 relationship.

172 2.6. Determination of PTX encapsulation efficiency

173 The prepared BSA-PTX solution (320 μ L) was pipetted into a centrifuge tube and
174 to this solution, 2 mL of dichloromethane was added and vortexed for 5 min; the
175 solution was then left to equilibrate for 15 min. The obtained solution was filtered
176 through a 0.22 μ m syringe filter and transferred to a 1 mL penicillin bottle. The
177 ultrafiltrate (20 μ L) was injected into the HPLC system and analysed at a UV
178 absorption wavelength of 227 nm; the content of PTX detected was called the content
179 of free drug. Encapsulation efficiency (EE) was calculated according to the following
180 equation

$$181 \quad EE(\%) = \frac{W_{\text{total}} - W_{\text{free}}}{W_{\text{total}}} \quad (1)$$

182 where W_{free} is the amount of free drug and W_{total} is the amount of total drug.

183 2.7. Determination of the conversion rate of albumin

184 The BSA-PTX solution (4 mL) was pipetted into a centrifuge tube and centrifuged
185 at 10,000 rpm for 30 min at 4 °C. Subsequently, 50 μ L of the supernatant was pipetted
186 out and added to 1950 μ L of purified water. The ultraviolet absorption of this solution
187 was measured at 227 nm and the corresponding chromatogram was recorded. The
188 recorded value represents absorbance by free albumin and was used to calculate the
189 conversion of BSA-PTX nanoparticles. A linear regression equation, $Y = 0.632X +$
190 0.0245 ($R^2 = 0.9991$) was obtained, where the absorbance (Y) and albumin
191 concentration (X) exhibited a good linear relationship in the concentration range of 10–
192 100 μ g/mL. The albumin conversion rate(ACR) was calculated according to the
193 following equation:

$$194 \quad ACR(\%) = \frac{W_{\text{total}} - W_{\text{free}}}{W_{\text{total}}} \quad (2)$$

195 where W_{free} is the amount of free albumin and W_{total} is the amount of total albumin.

196 2.8. Measurement of particle size of nanoparticles

217 Albumin nanoparticles powders were dispersed with pure water and their mean
218 size were characterised using a laser particle-size analyser (Nano ZS90 Malvern
219 Instruments, UK).

200 2.9. Fourier transform infrared (FTIR) spectroscopy

201 The FTIR spectra of the samples were obtained on a Nicolet 6700 FTIR
202 spectrometer (Thermo Scientific, Waltham, MA, USA). Each sample was mixed with
203 potassium bromide in an agate mortar and compressed into a thin disc to form
204 pelletised specimens. These specimens were scanned in the range of 4000–400 cm⁻¹
205 at a resolution of 4 cm⁻¹.

206 2.10. Raman spectrometry (RS)

207 FT-Raman spectra were acquired on a Nicolet 6700 FTIR with NXR FT-Raman
208 module (1064 nm) in the wavenumber range of 4000–400 cm⁻¹ over 64 scans with a
209 4 cm⁻¹ spectral resolution.

210 2.11. Differential scanning calorimetry (DSC)

211 DSC measurements were conducted on an HSC-1 DSC scanning calorimeter
212 (Hengjiu Instrument Ltd., Beijing, China). Samples (15 mg) were placed in aluminium
213 pans, sealed using the sample pan press, and heated from 25 to 400 °C at a rate of
214 10 °C/min in a nitrogen atmosphere.

215 2.12. X-ray diffraction (XRD)

216 The structural properties of the samples were analysed using a D8 Focus X-Ray
217 diffractometer (Bruker, Germany) with Cu-K α radiation operating at 40 kV and 40 mA.
218 The samples were scanned in the 2 θ range of 3° to 90° at 0.02°/min.

219 2.13. Scanning electron microscopy (SEM)

220 The samples were fixed on a SEM stub with a conductive carbon tape and sputter-
221 coated with a thin layer of gold using an SBC-12 sputter-coater (KYKY Tech. Ltd.,
222 Beijing, China). The surface morphology of the samples was then observed using a

223 S-4300 scanning electron microscope (Hitachi, Tokyo, Japan).

224 2.14. Transmission electron microscopy (TEM)

225 Nanoparticle shape and morphology were observed using a transmission electron
226 microscope (Hitachi HT7700, Japan) operating at an accelerating voltage of 100 kV.
227 The nanoparticle suspension was obtained by adding 5 mg of nanoparticles powder
228 to 5 mL of purified water at room temperature, vortexed for 10 s, and equilibrated for
229 30 s. From this solution, a drop was withdrawn with a micropipette and placed on a
230 carbon-coated copper grid. Excess suspension was blotted from the grid with a filter
231 paper. The remaining deposit was negatively stained with 1% phosphotungstic acid
232 (w/w, pH 7.1). The excess was removed with a filter paper and the deposit was dried
233 before analysis.

234 2.15. In vitro drug release

235 PTX release from the nanoparticles was analysed using the slurry method at ($37 \pm$
236 0.5) °C. BSA-PTX nanoparticles were dissolved in 100 mL of a phosphate buffer
237 solution (PBS, pH 7.4, 37 °C) by stirring at 100 rpm. At predetermined time intervals,
238 2 mL of the release medium was removed and replaced with an equal amount of fresh
239 release medium to maintain sink conditions, 2 mL alcohol was added, and filtered
240 through a 0.45 µm cellulose acetate membrane. The released drug content was
241 analysed at 227 nm by HPLC (LC-1000D HPLC, Shandong Lunan Ruihong Chemical
242 Instrument Co. Ltd.). Measurements were carried out in triplicate to calculate
243 cumulative drug release.

244 2.16. Cell uptake of the prepared nanoparticles

245 To determine the specific affinity of PTX-BSA and FA-BSA-PTX towards FR, FITC
246 was encapsulated in these two systems and LCSM was conducted to evaluate if the
247 uptake of FA-BSA-PTX by HeLa cells was enhanced using FR. HeLa cells were plated
248 at a density of 1.0×10^6 cells/well and cultured overnight at 37 °C. Subsequently, the
249 culture medium was discarded. Free FITC, FITC-BSA-PTX, and FITC-FA-BSA-PTX
250 were diluted in the serum-free medium and each sample was added to two wells and

251 incubated at 37 °C for 3 h. The cells were finally washed thrice with PBS, and analysed
252 using LCSM to observe the uptake by HeLa cells.

253 2.17. Data analysis

254 Single correlation analysis was conducted to examine the effect of process
255 parameters on the properties of albumin nanoparticles. All statistical evaluations were
256 conducted with SPSS for Windows, version 17.0.0 (SPSS Inc., USA). A value of $p <$
257 0.05 was considered to be statistically significant.

258 3. Results and discussion

259 3.1. Coagulant screening

260 According to the available literature, intermolecular functional regions can be
261 generated by interactions between protein molecules and divalent metal ions to form
262 precipitates and these precipitates enhance the stability and duration of protein
263 interaction, resulting in a sustained release effect [27]. Moreover, the impact may be
264 caused by the type of coagulant on the crosslinking mechanism and rate, thereby
265 affecting the particle size and conversion rate of albumin nanoparticles. Taking these
266 factors into account, in this study, the effect of different coagulants on the particle size
267 and conversion rate was investigated.

268 As shown in Fig. 2, under the same preparation conditions, the conversion rate of
269 the 50 mg coagulant group (1.25 mg/mL) was higher than that of 20 mg coagulant
270 group (0.5 mg/mL). In terms of the conversion rate in the 0.5 mg/mL coagulant group,
271 the following order was observed – magnesium chloride > gluconolactone > calcium
272 chloride > calcium lactate, with magnesium chloride resulting in the highest conversion
273 rate (47%). In the case of the 1.25 mg/mL coagulant group, the observed order was
274 magnesium chloride > gluconolactone > calcium chloride > calcium lactate, with
275 magnesium chloride resulting in the highest conversion rate (84.5%). Significant
276 nanoparticle flocculation was observed when gluconolactone was used as the
277 coagulant, owing to which the nanoparticles could not be effectively dispersed.

278 The particle size of albumin nanoparticles in the 0.5 mg/mL coagulant group was
 279 smaller than that in the 1.25 mg/mL group. Particle-size order in the 0.5 mg/mL
 280 coagulant group was magnesium chloride < calcium chloride < calcium lactate <
 281 gluconolactone, with nanoparticles prepared using magnesium chloride being the
 282 smallest (310.6 nm). In the 1.25 mg/mL coagulant group, the particle-size order was
 283 magnesium chloride < calcium chloride < calcium lactate < gluconolactone, with
 284 nanoparticles prepared using magnesium chloride being the smallest (398.6 nm).

285 Thus, considering the particle-size and conversion-rate indicators, magnesium
 286 chloride was selected as the optimal coagulant and used in the rest of the study.

287 3.3. Effect of process parameters on the properties of albumin nanoparticles

288 During the synthesis of albumin nanoparticles by HPHCM, nanoparticle size,
 289 albumin-conversion rate, and encapsulation rate can be adjusted by controlling the
 290 operating conditions such as BSA concentration, coagulant dosage, and
 291 homogenisation time. Therefore, we investigated the effect of different experimental
 292 conditions (Table 1) on the quality of the produced nanoparticles.

293 The effect of BSA concentration on the synthesised albumin nanoparticles is
 294 illustrated in Fig. 3a. As the BSA concentration increased from 5 to 40 mg/mL, particle
 295 size gradually increased from 327 to 377 nm. The change in particle size can be
 296 explained using the following relationships:

$$297 \quad J = A \exp^{(-B/(\ln S)^2)} \quad (3)$$

$$298 \quad A = N_0 v \quad (4)$$

$$299 \quad B = \frac{16\pi\sigma^3 V_s^2}{3k^3 T^3} \quad (5)$$

$$300 \quad v = \frac{kT}{3\pi a^3 \eta} \quad (6)$$

304 where S is the degree of supersaturation, J is the nucleation rate, N_0 is the initial
305 number of molecules of solute per unit volume, v is the frequency of molecular
306 transport to the solid-liquid interface, Furthermore, K is the Boltzmann constant and T
307 represents temperature. σ indicates interfacial tension at the solid-liquid interface, and
308 V_s is the volume of solute molecules. η is the viscosity of the surrounding solution, and
309 a is the mean effective diameter of the diffusing species.

310 Using Equation (3), it was found that viscosity increased as the BSA concentration
311 increased. Larger particles were produced by slowing the nucleation due to a reduced
312 protein transport between water and ethanol. In addition, higher protein concentrations
313 led to greater supersaturation (Equation (4)), resulting in small nuclei. However, there
314 is a greater chance of particle collision due to high supersaturation resulting in
315 solidification, thus producing larger nanoparticles [28]. It has been reported by
316 Prajapati et al. that coagulation occurs as BSA concentration increases, resulting in
317 larger particles [29]. Albumin conversion initially increased and then decreased, with
318 the highest conversion rate (45.8%) observed at a BSA concentration of 10 mg/mL.
319 Shu et al. described that the conversion rate increased with an increase in BSA
320 concentration in the range of 0.5–3 mg/mL [30]. In the current study, however, the low
321 conversion rate observed at high concentrations may be attributed to the
322 supersaturation effect, as described earlier. Meanwhile, the encapsulation efficiency
323 varied from 85.3% to 90.8%, with no obvious trend. Statistically, the influence of BSA
324 concentration on particles size was highly significant ($p < 0.01$) and exerted a large
325 influence on albumin-conversion rate ($p < 0.05$) into nanoparticles.

326 The effect of magnesium chloride concentration on the properties of albumin
327 nanoparticles is illustrated in Fig. 3b. As the concentration of $MgCl_2$ increased,
328 nanoparticle size, conversion rate, and encapsulation rate increased gradually. An
329 increase in the number of coagulant molecules resulted in an increase in the
330 nucleation rate, which in turn increased the particle size and conversion rate.

331 The effect of water/ethanol volume ratio on albumin nanoparticles is shown in Fig.
332 3c. As the water/ethanol volume ratio decreased from 30 to 10, the particle size initially

333 decreased and then increased. The minimum particle size of 323 nm was observed at
334 water/ethanol = 25/1, which is consistent with previously reported results [31].
335 Meanwhile, the BSA conversion rate decreased when the water/ethanol volume ratio
336 decreased from 30 to 10. The encapsulation rate initially increased and then
337 decreased and the highest value (92.2%) was observed at water/ethanol = 20/1.

338 The effect of homogenisation pressure on the properties of BSA nanoparticles is
339 shown in Fig. 3d. As the pressure increased from 600 to 1000 bar, particle size initially
340 decreased and then increased, with the smallest particles (302 nm) being obtained at
341 800 bar. It is well known that a homogeniser gradually warms up during operation and
342 rapid reactant consumption occurs as the reaction rate increases at higher
343 temperatures. As a result, the reactants are depleted, resulting in the formation of
344 smaller nanoparticles at higher temperatures [32]. These results are consistent with
345 those of Jennings et al. [33]. Later, the particle size increased gradually due to the
346 exaggerated pressure of the homogeniser, an exorbitant instantaneous energy, and
347 the solidification of particles [34]. In this process, the conversion rate also increased.
348 Statistically, the influence of homogenisation pressure on conversion rate was highly
349 significant ($p < 0.01$). The encapsulation rate initially increased and then decreased,
350 reaching the highest value (89.7%) at a homogenisation pressure of 700 bar.

351 The effect of homogenisation time on albumin nanoparticles is illustrated in Fig. 3e.
352 When the homogenisation time increased from 3 to 9 min, the particle size increased
353 gradually while in the range of 9–15 min, it increased rapidly. This phenomenon can
354 be attributed to an energy barrier between the particles. When individual particles
355 approach each other, the attractive potential energy (EA) increases rapidly, whereas
356 the repulsive potential energy (ER) changes more slowly. Generally speaking, there is
357 a maximum value (E_{max}) in the total potential energy curve, which represents the
358 energy barrier and prevents particles from absorbing each other. The E_{max} may be
359 overcome when the particles approach each other. As the homogenisation time
360 increases, more and more energy is accumulated. After 9 min, the repulsive potential
361 energy, E_{max} , could be overcome, owing to which individual nanoparticles were

362 strongly attracted to each other, resulting in a sudden increase in particle size.
363 Statistically, the influence of homogenisation time on particle size was found to be
364 significant ($p < 0.05$). Furthermore, the conversion rate increased as the
365 homogenisation time increased. Meanwhile, the encapsulation rate increased initially
366 and then decreased, with the maximum value (91.4%) observed at 12 min.

367 The effect of the BSA/PTX ratio on albumin nanoparticles is shown in Fig. 3f. When
368 the BSA/PTX ratio decreased from 25 to 5 (dosage increases), the conversion rate
369 and particle size increased; however, the encapsulation efficiency decreased. This
370 indicates that the amount of BSA was not sufficient to encapsulate the entire loaded
371 PTX amount. Similarly, when the dosage increased, the drug acted as a coagulant,
372 resulting in many crystalline nuclei. At this time, BSA was adsorbed, resulting in
373 particle adherence and large particles [35]. Statistically, the BSA/PTX ratio was found
374 to significantly influence the encapsulation efficiency ($p < 0.05$).

375 Finally, the following reaction conditions were deemed to be optimal – BSA
376 concentration = 10 mg/mL, $MgCl_2$ = 0.5 mg/mL, water/ethanol volume ratio = 20/1,
377 homogenisation pressure = 800 bar, homogenisation time = 3 min, and BSA/PTX =
378 10/1.

379 3.4. Electron microscope analysis

380 The morphology of BSA-PTX nanoparticles were analysed using TEM and SEM,
381 as shown in Fig. 4. It can be seen in the SEM images (Fig. 4a) that albumin is in the
382 form of irregular flakes while raw PTX is in the form of crystalline strips (Fig. 4b). It can
383 also be concluded from the SEM images (Fig. 4c and d) of BSA-PTX nanoparticles
384 that the freeze-dried particles were mostly in the form of dimers and trimers with an
385 average particle size of 300 nm; in terms of shape, most single particles were spherical.
386 The TEM image of BSA-PTX nanoparticles (Fig. 4f) shows that the freeze-dried
387 powder consisted of nearly spherical nanoparticles with an average particle size of
388 300 nm. It can be seen in the partial image (Fig. 4e) that there are obvious black
389 crystals in the middle of the particles; these are assumed to be cores formed by $MgCl_2$

390 (coagulant). During the formation of albumin nanoparticles, the coagulant formed the
391 core and albumin shells were formed around them. Faint PTX crystal strips could also
392 be observed, implying that PTX was dispersed in the carrier in the form of crystals.

393 3.5. FTIR analysis

394 FTIR can be used to easily detect the relative intensity of amide bands in proteins,
395 thus allowing us to analyse their structure. We employed FTIR to analyse the structure
396 of albumin nanoparticles and investigate changes in their characteristic absorption
397 peaks to determine their composition (Fig. 5). The IR spectrum of albumin included
398 characteristic peaks at 1638, 1540, and 1238 cm^{-1} , representing amide I (1600–1700
399 cm^{-1} , C=O stretching vibrations), amide II (1500–1600 cm^{-1} , N-H in-plane bending and
400 C-N stretching), and amide III (1220–1280 cm^{-1} , C-N stretching and N-H in-plane
401 bending) groups, respectively. The appearance of these peaks is mainly due to the
402 fact that albumin is in a disordered coiled state [36]. It can be seen from the figure that
403 the absorption band of amide I moved from 1638 to 1654 cm^{-1} after albumin was
404 micronised, which may be due to the rearrangement of amino and carboxyl hydrogen
405 bonds on the BSA peptide chain during the homogenisation process. Protein
406 conformation undergoes changes once hydrogen bonds, which are the main forces
407 responsible for the double helix structure in a protein, change [37]. No obvious
408 changes could be observed in the FTIR spectrum of BSA, but the peak intensity
409 corresponding to amide II (1540 cm^{-1}) increased significantly, indicating that the C-N
410 and/or NH bonds underwent changes due to interactions between different functional
411 groups [38]. An obvious characteristic peak could be observed in the FTIR spectrum
412 of MgCl_2 at 2250 cm^{-1} ; however, it could not be observed in the spectra of magnesium
413 chloride blank nanoparticles and magnesium chloride drug-loaded nanoparticles. This
414 implies that the MgCl_2 amount is so small that it has little effect on drug-loaded
415 nanoparticles. The PTX spectrum included a ketocarbonyl (C=O) stretching vibration
416 peak at 1733 cm^{-1} , which could also be observed in the spectrum of magnesium
417 chloride drug-loaded nanoparticles. Thus, FTIR validated PTX encapsulation in
418 albumin.

419 3.6. Raman spectroscopy analysis

420 Raman spectroscopy is a rapid, simple, repeatable, and non-destructive qualitative
421 and quantitative technique that does not require special sample preparation. Thus, we
422 employed this method to analyse the BSA-based nanoparticles prepared in this study.
423 As shown in Fig. 6, peaks were observed at 1655 and 1339 cm^{-1} in the spectrum
424 corresponding to albumin, representing amide I and II groups [39]. After nanoparticle
425 formation, the relative intensities of these peaks decreased. This phenomenon can be
426 explained by the structural changes occurring during the formation of BSA
427 nanoparticles [40]. S-S stretching vibrations were observed in the wavenumber range
428 of 500–550 cm^{-1} and these can be used to evaluate the configuration characteristics
429 of disulphide bonds. The Raman peak at 510 cm^{-1} is characteristic of the twist-twist-
430 twist configuration. Upon nanoparticle formation, Raman peaks were observed at 525
431 cm^{-1} corresponding to twist-twist-trans and trans-twist-twist configurations, indicating
432 changes in the disulphide bond configuration and protein structure.

433 3.7. Differential scanning calorimetry analysis

434 The DSC curves of BSA, magnesium chloride, magnesium chloride blank
435 nanoparticles, magnesium chloride drug-loaded nanoparticles, and PTX are shown in
436 Fig. 7. A wide endothermic peak could be observed in the thermogram of albumin at
437 ~ 222 °C; however, this peak shifted to 197 °C and widened in the thermogram of
438 magnesium chloride drug-loaded nanoparticles. Data analysis showed that albumin
439 was denatured during nanoparticle formation, which is consistent with related reports
440 [41]. PTX exhibited an endothermic peak at ~ 219 °C, which corresponds to its melting
441 point, indicating that the drug exists in a crystalline state. However, no characteristic
442 endothermic peaks could be observed at this temperature in the thermogram of BSA-
443 PTX nanoparticles, indicating that the drug underwent phase transformation and
444 converted into an amorphous structure (low drug contents might also be responsible
445 for this observation). It is well known that polymers retard crystalline growth in drugs
446 via surface adsorption. Thus, the disappearance of the PTX melting peak indicates
447 that PTX crystallisation was inhibited by albumin during precipitation [42].

448 3.8. X-ray diffraction analysis

449 XRD was conducted to investigate structural changes in the drug and albumin
450 during nanoparticle preparation (Fig. 8). Pure PTX exhibited a strong diffraction peak,
451 indicating its crystalline nature. In contrast, BSA was present in an amorphous state,
452 as described in other studies [43]. Multiple diffraction peaks can be seen in the XRD
453 patterns of blank and drug-loaded nanoparticles, which is not the case in the XRD
454 patterns of albumin nanoparticles obtained by different methods. This difference might
455 be due to the binding of MgCl₂ and albumin [44,45]. Furthermore, the original
456 diffraction peaks of PTX could not be observed in the XRD patterns of the
457 nanoparticles, suggesting that drug converted into an amorphous state [46].

458 3.9. In vitro drug release

459 The effect of different crosslinking agents (genipin, vanillin, and glutaraldehyde) on
460 drug release from the nanoparticles in in vitro conditions was investigated [47],[48].
461 BSA-PTX nanoparticles were immersed in PBS (pH 7.4) at 37 °C for 24 h in vitro and
462 the amount of drug released was analysed (Fig. 9). While genipin (20 mg) and vanillin
463 (13.45 mg) and glutaraldehyde (1.6 mL, 0.1%) was added at a concentration of 4
464 µL/mg albumin; the crosslinking time was set at 3 h. A sustained release could be
465 observed with crosslinked BSA-PTX nanoparticles, whereas non-crosslinked BSA-
466 PTX nanoparticles exhibited a rapid release, with a 37% initial release within 15 min.
467 The release rate reached 97% within 4 h after which it converted into a plateau. When
468 the nanoparticles were in contact with the release medium, the drug adsorbed on
469 nanoparticle surfaces was first dissolved and released, resulting in a burst-release
470 effect. At 1 h, the cumulative release rate was in the range of 42.61% to 59.32%.
471 Subsequently, the release rate increased to 82.92% to 91.70% within 6 h, after which
472 it gradually slowed down (plateau phase). The release mode was biphasic, i.e., a burst
473 effect at the beginning followed by a slow release phase [49]. The release medium
474 continuously penetrated the interior of the nanoparticles, resulting in the release of
475 drug molecules embedded in their bulk. The dissolved drug diffused into the medium
476 through carriers depending on the drug-concentration gradient inside and outside the

477 particles; when accompanied by the slow dissolution of the carrier material, this
478 resulted in a slow release. Such sustained release behaviour can be attributed to the
479 decrease in the free volume of the matrix treated with the crosslinking agents and
480 $MgCl_2$, which may limit the diffusion of drugs into the protein network [27]. The
481 observed release rate followed the trend, genipin group > glutaraldehyde group >
482 vanillin group.

483 3.10. Cell uptake of BSA-based nanoparticles

484 The results of in vitro cell-uptake studies on BSA-based nanoparticles are
485 illustrated in Fig. 10. Fluorescence could be clearly observed in the case of FITC-FA-
486 BSA-PTX (Fig. 10A) nanoparticles when incubated with HeLa cells at 37 °C for 3 h,
487 while FITC-BSA-PTX (Fig. 10B) exhibited a relatively weak fluorescence. In addition,
488 fluorescence was absent in the case of FITC (Fig. 10C). It can be concluded from
489 these observations that FA mediated the endocytosis of BSA-NP in HeLa cells with a
490 high FR expression, which increased the number of nanoparticles entering the cells.
491 In contrast, samples without folate coupling had no such function. The amount of
492 folate-modified nanoparticles entering HeLa cells was significantly high. Therefore, it
493 can be stated that FA can be used as a targeting ligand to enhance the active targeting
494 effect of albumin nanoparticles on HeLa cells with a high FR expression.

495 4. Conclusion

496 In this study, a new green method, called HPHCM, was developed for the
497 preparation of albumin nanoparticles. The effect of different coagulants on the particle
498 size and conversion rate of albumin nanoparticles was evaluated and it was found that
499 $MgCl_2$ resulted in small particles and a high albumin-conversion rate. It was proved by
500 single-factor experiments that BSA concentration, coagulant concentration, and
501 homogenisation time influence the size of albumin nanoparticles, albumin-conversion
502 rate, and encapsulation rate. SEM analysis indicated that the prepared albumin
503 nanoparticles were spherical with an average size of 300 nm and easily formed dimers
504 or trimers upon lyophilisation. DSC testing showed that albumin mainly existed in an

505 amorphous form after nanoparticle formation. The peak shift corresponding to amide
506 I in the FTIR spectrum of the nanoparticles is evidence of changes in protein
507 conformation. Using Raman spectroscopy, these changes were ascribed to changes
508 in the disulphide bond configuration and protein structure. In vitro release studies
509 confirmed sustained release from crosslinked BSA-PTX nanoparticles for over 6 h. In
510 terms of the crosslinking agent, the release rate followed the order genipin >
511 glutaraldehyde > vanillin. In vitro studies also showed that FA can be used as a
512 targeting ligand for albumin carriers to enhance the active targeting effect of BSA-PTX
513 nanoparticles on HeLa cells with a high FR expression. Finally, HPHCM is a simple
514 and feasible method with great potential to synthesise drug carriers. It should be noted
515 that BSA was used in this study with only four coagulants and three cross-linking
516 agents. Therefore, other kinds of albumin, coagulants, and cross-linking agents should
517 also be studied to develop efficient drug carriers for targeted delivery.

518

519 **Abbreviations**

520 PTX: Paclitaxel; BSA: Bovine serum albumin; FA: Folic acid; HPHCM: high-pressure
521 homogenisation coagulation method; DSC: Differential scanning calorimetry; XRD:
522 X-ray diffraction; FTIR: Fourier transform infrared spectroscopy; TEM: Transmission
523 electron microscopy; EE: Encapsulation efficiency; ACR: Albumin conversion rate

524 **Acknowledgements**

525 The authors gratefully acknowledge the financial supports of the National Natural
526 Science Foundation of China (Grant No. 21908119) and the Natural Science
527 Foundation of Heilongjiang Province of China (Grant No. H2016097).

528 **Authors' Contributions**

529 CY, LT, SX participated in the design of the study. CY, LT, SX, CS, PH, QJ and HC
530 performed the experiments and materials characterization. CY, LT and SX drafted
531 the manuscript. All authors read and approved the final manuscript.

532 **Authors' Information**

533 All authors (Dr. Xiaoyu Sui, Dr. Tingting Liu, Dr. Cuiyan Han, Yan Chu, Shuo Chai,
534 Hong Pan and Jiayi Qian) are from Qiqihar Medical University, China.

535 **Competing Interests**

536 The authors declare that they have no competing interests.

537

538

References

- 539 1. Bansal A, Kapoor DN, Kapil R, et al (2011) Design and development of
540 paclitaxel-loaded bovine serum albumin nanoparticles for brain targeting. *Acta*
541 *Pharm* 61:141–156.
- 542 2. Dang Y, Guan J (2020) Nanoparticle-based drug delivery systems for cancer
543 therapy. *Smart Mater Med* 1:10–19.
- 544 3. Thao LQ, Byeon HJ, Lee C, et al (2016) Doxorubicin-Bound Albumin
545 Nanoparticles Containing a TRAIL Protein for Targeted Treatment of Colon
546 Cancer. *Pharm Res* 33:615–626.
- 547 4. Karami E, Behdani M, Kazemi-Lomedasht F (2020) Albumin nanoparticles as
548 nanocarriers for drug delivery: Focusing on antibody and nanobody delivery
549 and albumin-based drugs. *J Drug Deliv Sci Technol* 55:101471.
- 550 5. Bora DK, Deb P (2009) Fatty acid binding domain mediated conjugation of
551 ultrafine magnetic nanoparticles with albumin protein. *Nanoscale Res Lett*
552 4:138–143.
- 553 6. Kratz F (2008) Albumin as a drug carrier: Design of prodrugs, drug conjugates
554 and nanoparticles. *J Control Release* 132:171–183.
- 555 7. Zu Y, Meng L, Zhao X, et al (2013) Preparation of 10-hydroxycamptothecin-
556 loaded glycyrrhizic acid-conjugated bovine serum albumin nanoparticles for
557 hepatocellular carcinoma-targeted drug delivery. *Int J Nanomedicine* 8:1207–
558 1222.
- 559 8. Yewale C, Baradia D, Vhora I, Misra A (2013) Proteins: Emerging carrier for
560 delivery of cancer therapeutics. *Expert Opin Drug Deliv* 10:1429–1448.
- 561 9. Gong T, Tan T, Zhang P, et al (2020) Palmitic acid-modified bovine serum
562 albumin nanoparticles target scavenger receptor-A on activated macrophages
563 to treat rheumatoid arthritis. *Biomaterials* 258:120296.

- 564 10. Kudarha RR, Sawant KK (2017) Albumin based versatile multifunctional
565 nanocarriers for cancer therapy: Fabrication, surface modification, multimodal
566 therapeutics and imaging approaches. *Mater Sci Eng C* 81:607–626.
- 567 11. Zhao D, Zhao X, Zu Y, et al (2010) Preparation, characterization, and in vitro
568 targeted delivery of folate-decorated paclitaxel-loaded bovine serum albumin
569 nanoparticles. *Int J Nanomedicine* 5:669–677.
- 570 12. Ling D, Hackett MJ, Hyeon T (2014) Surface ligands in synthesis, modification,
571 assembly and biomedical applications of nanoparticles. *Nano Today* 9:457–
572 477.
- 573 13. Nosrati H, Abbasi R, Charmi J, et al (2018) Folic acid conjugated bovine serum
574 albumin: An efficient smart and tumor targeted biomacromolecule for inhibition
575 folate receptor positive cancer cells. *Int J Biol Macromol* 117:1125–1132.
- 576 14. Akbarian A, Ebtekar M, Pakravan N, Hassan ZM (2020) Folate receptor alpha
577 targeted delivery of artemether to breast cancer cells with folate-decorated
578 human serum albumin nanoparticles. *Int J Biol Macromol* 152:90–101.
- 579 15. Qi L, Guo Y, Luan J, et al (2014) Folate-modified bexarotene-loaded bovine
580 serum albumin nanoparticles as a promising tumor-targeting delivery system. *J*
581 *Mater Chem B* 2:8361–8371.
- 582 16. Zhang L, Hou S, Mao S, et al (2004) Uptake of folate-conjugated albumin
583 nanoparticles to the SKOV3 cells. *Int J Pharm* 287:155–162.
- 584 17. Steinhauser IM, Langer K, Strebhardt KM, Spänkuch B (2008) Effect of
585 trastuzumab-modified antisense oligonucleotide-loaded human serum albumin
586 nanoparticles prepared by heat denaturation. *Biomaterials* 29:4022–4028.
- 587 18. Yang R, Zheng Y, Wang Q, Zhao L (2018) Curcumin-loaded chitosan–bovine
588 serum albumin nanoparticles potentially enhanced A β 42 phagocytosis and
589 modulated macrophage polarization in Alzheimer’s disease. *Nanoscale Res*
590 *Lett* 13:1–9.

- 591 19. Müller BG, Leuenberger H, Kissel T (1996) Albumin nanospheres as carriers
592 for passive drug targeting: An optimized manufacturing technique. *Pharm.*
593 *Res.* 13:32–37
- 594 20. Jahanban-Esfahlan A, Dastmalchi S, Davaran S (2016) A simple improved
595 desolvation method for the rapid preparation of albumin nanoparticles. *Int J*
596 *Biol Macromol* 91:703–709.
- 597 21. Langer K, Balthasar S, Vogel V, et al (2003) Optimization of the preparation
598 process for human serum albumin (HSA) nanoparticles. *Int J Pharm* 257:169–
599 180.
- 600 22. Koenig SG, Dillon B (2017) Driving toward greener chemistry in the
601 pharmaceutical industry. *Curr Opin Green Sustain Chem* 7:56–59.
- 602 23. Sharma RK, Gulati S, Mehta S (2012) Preparation of gold nanoparticles using
603 tea: A green chemistry experiment. *J Chem Educ* 89:1316–1318.
- 604 24. Karthika S, Radhakrishnan TK, Kalaichelvi P (2020) Crystallization and Kinetic
605 Studies of an Active Pharmaceutical Compound Using Ethyl Lactate As a
606 Green Solvent. *ACS Sustain Chem Eng* 8:1527–1537.
- 607 25. Yew YP, Shameli K, Miyake M, et al (2016) Green Synthesis of Magnetite
608 (Fe₃O₄) Nanoparticles Using Seaweed (*Kappaphycus alvarezii*) Extract.
609 *Nanoscale Res Lett* 11:012-014.
- 610 26. Sun Y, Zhao Y, Teng S, et al (2019) Folic acid receptor-targeted human serum
611 albumin nanoparticle formulation of cabazitaxel for tumor therapy. *Int J*
612 *Nanomedicine* 14:135–148.
- 613 27. Wang W, Lei Y, Sui H, et al (2017) Fabrication and evaluation of nanoparticle-
614 assembled BSA microparticles for enhanced liver delivery of glycyrrhetic
615 acid. *Artif Cells, Nanomedicine Biotechnol* 45:740–747.
- 616 28. Galisteo-González F, Molina-Bolívar JA (2014) Systematic study on the

- 617 preparation of BSA nanoparticles. *Colloids Surfaces B Biointerfaces* 123:286–
618 292.
- 619 29. Prajapati A, Srivastava A (2019) Preparation, Characterization and
620 Encapsulation Efficiency of Egg Albumin Nanoparticles Using EDC as
621 Crosslinker. *J Sci Ind Res* 78:703–705
- 622 30. Shu S, Zhang X, Teng D, et al (2009) Polyelectrolyte nanoparticles based on
623 water-soluble chitosan-poly(l-aspartic acid)-polyethylene glycol for controlled
624 protein release. *Carbohydr Res* 344:1197–1204.
- 625 31. Dang F, Enomoto N, Hojo J, Enpuku K (2009) Sonochemical synthesis of
626 monodispersed magnetite nanoparticles by using an ethanol-water mixed
627 solvent. *Ultrason Sonochem* 16:649–654.
- 628 32. Mohammed Fayaz A, Balaji K, Kalaichelvan PT, Venkatesan R (2009) Fungal
629 based synthesis of silver nanoparticles-An effect of temperature on the size of
630 particles. *Colloids Surfaces B Biointerfaces* 74:123–126.
- 631 33. Jennings V, Lippacher A, Gohla SH (2002) Medium scale production of solid
632 lipid nanoparticles (SLN) by high pressure homogenization. *J Microencapsul*
633 19:1–10.
- 634 34. Yazdani F, Edrissi M (2010) Effect of pressure on the size of magnetite
635 nanoparticles in the coprecipitation synthesis. *Mater Sci Eng B Solid-State*
636 *Mater Adv Technol* 171:86–89.
- 637 35. Yang L, Cui F, Cun D, et al (2007) Preparation, characterization and
638 biodistribution of the lactone form of 10-hydroxycamptothecin (HCPT)-loaded
639 bovine serum albumin (BSA) nanoparticles. *Int J Pharm* 340:163–172.
- 640 36. Tang J, Luan F, Chen X (2006) Binding analysis of glycyrrhetic acid to
641 human serum albumin: Fluorescence spectroscopy, FTIR, and molecular
642 modeling. *Bioorganic Med Chem* 14:3210–3217.

- 643 37. Shi XJ, Li D, Xie J, et al (2012) Spectroscopic investigation of the interactions
644 between gold nanoparticles and bovine serum albumin. *Chinese Sci Bull*
645 57:1109–1115.
- 646 38. Costa BC, Ximenes VF, Lisboa-filho PN (2017) Synthetic nanoparticles of
647 bovine serum albumin with entrapped salicylic acid. 11–21
- 648 39. Bhogale A, Patel N, Mariam J, et al (2014) *Colloids and Surfaces B :*
649 *Biointerfaces* Comprehensive studies on the interaction of copper
650 nanoparticles with bovine serum albumin using various spectroscopies.
651 *Colloids Surfaces B Biointerfaces* 113:276–284.
- 652 40. Rohiwal SS, Satvekar RK, Tiwari AP, et al (2015) Investigating the influence of
653 effective parameters on molecular characteristics of bovine serum albumin
654 nanoparticles. *Appl Surf Sci* 334:157–164.
- 655 41. Dinarvand R, Taheri A, Atyabi F, et al (2011) Nanoparticles of conjugated
656 methotrexate-human serum albumin: Preparation and cytotoxicity evaluations.
657 *J Nanomater* 2011:5.
- 658 42. Honary S, Jahanshahi M, Golbayani R, et al (2010) Doxorubicin-loaded
659 albumin nanoparticles: Formulation and characterization. *J Nanosci*
660 *Nanotechnol* 10:7752–7757.
- 661 43. Ruttala HB, Ramasamy T, Shin BS, et al (2017) Layer-by-Layer Assembly of
662 Hierarchical Nanoarchitectures to Enhance the Systemic Performance of
663 Nanoparticle Albumin-bound Paclitaxel. Elsevier B.V.
- 664 44. Wang D, Liang N, Kawashima Y, et al (2019) Biotin-modified bovine serum
665 albumin nanoparticles as a potential drug delivery system for paclitaxel. *J*
666 *Mater Sci* 54:8613–8626.
- 667 45. Zhao Y, Cai C, Liu M, et al (2020) Drug-binding albumins forming stabilized
668 nanoparticles for co-delivery of paclitaxel and resveratrol: In vitro/in vivo
669 evaluation and binding properties investigation. *Int J Biol Macromol* 153:873–

670 882.

671 46. Ruttala HB, Ko YT (2015) Liposome encapsulated albumin-paclitaxel
672 nanoparticle for enhanced antitumor efficacy. *Pharm Res* 32:1002–1016.

673 47. Elzoghby AO, Samy WM, Elgindy NA (2012) Albumin-based nanoparticles as
674 potential controlled release drug delivery systems. *J Control Release* 157:168–
675 182.

676 48. Song F, Zhang LM, Yang C, Yan L (2009) Genipin-crosslinked casein
677 hydrogels for controlled drug delivery. *Int J Pharm* 373:41–47.

678 49. Sahin S, Selek H, Ponchel G, et al (2002) Preparation, characterization and in
679 vivo distribution of terbutaline sulfate loaded albumin microspheres. *J Control*
680 *Release* 82:345–358.

681

682 **Figure legends**

683 Fig. 1. Schematic diagram of the experimental apparatus.①, High pressure
684 homogenizer; ②, Material cup; ③, Drug solution; ④, Peristaltic pump; ⑤, Heating
685 circulator bath.

686 Fig. 2. Influence of coagulant concentration and types of coagulants on the mean
687 particle size and BSA conversion efficiency.

688 Fig. 3. Influence of (a) BSA concentration (mg/mL), (b) MgCl₂ concentration (mg/mL),
689 (c) The volume ratio of water and ethanol, (d) Homogeneous pressure (bar), (e)
690 Homogeneous time (min) and (f) Mass ratio of BSA and PTX on the mean particle size,
691 encapsulation efficiency and total conversion.

692 Fig. 4. Scanning electron micrographs of BSA(a), PTX(b), BSA-PTX(c) and (d),
693 Transmission Electron Microscopy of BSA-PTX (e) and (f).

694 Fig. 5. FTIR spectra of BSA; MgCl₂; NP; PTX-BSA; and PTX. The characteristic
695 vibration bands related to BSA and PTX can be seen in the PTX-BSA NPs
696 nanoparticles.

697 Fig. 6. The DSC thermograms of BSA; MgCl₂; NP; PTX-BSA; and PTX .

698 Fig. 7. The XRD spectra of BSA ; MgCl₂; NP; PTX-BSA; and PTX .

699 Fig. 8. Raman spectrum of BSA; MgCl₂; NP; PTX-BSA; and PTX .

700 Fig. 9. In vitro release profiles of PTX from PTX-BSA. Crosslinking agent dosage,
701 glutaraldehyde/BSA 0.4 μl/mg; genipin/BSA 0.05 mg/mg; vanillin/BSA 0.02 mg/mg.

702 Fig.10. Laser scanning confocal microscope images of HeLa cells after incubation
703 with PTX-BSA. The LSCM images of the FITC-FA-BSA-PTX (A), FITC-BSA-PTX (B)
704 and FITC (C).

Figures

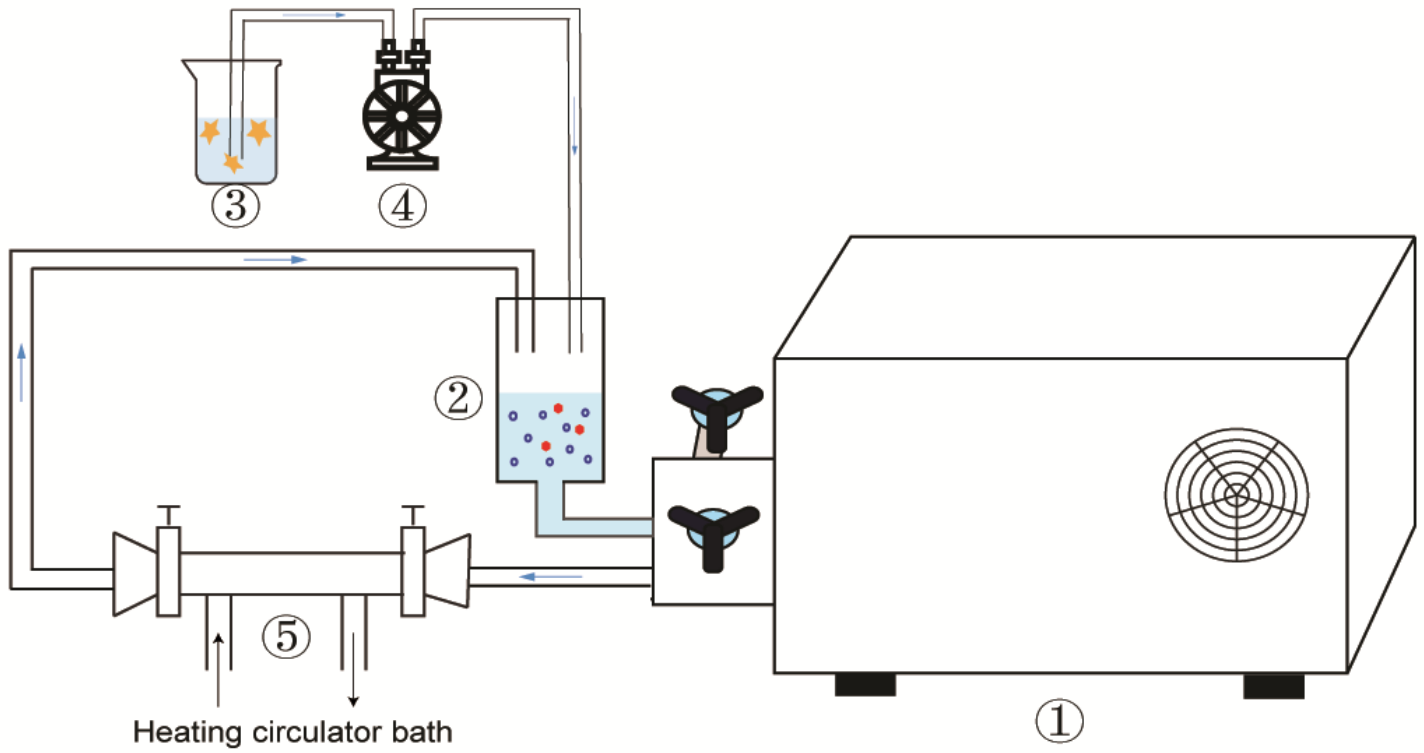


Figure 1

Schematic diagram of the experimental apparatus. ①, High pressure homogenizer; ②, Material cup; ③, Drug solution; ④, Peristaltic pump; ⑤, Heating circulator bath.

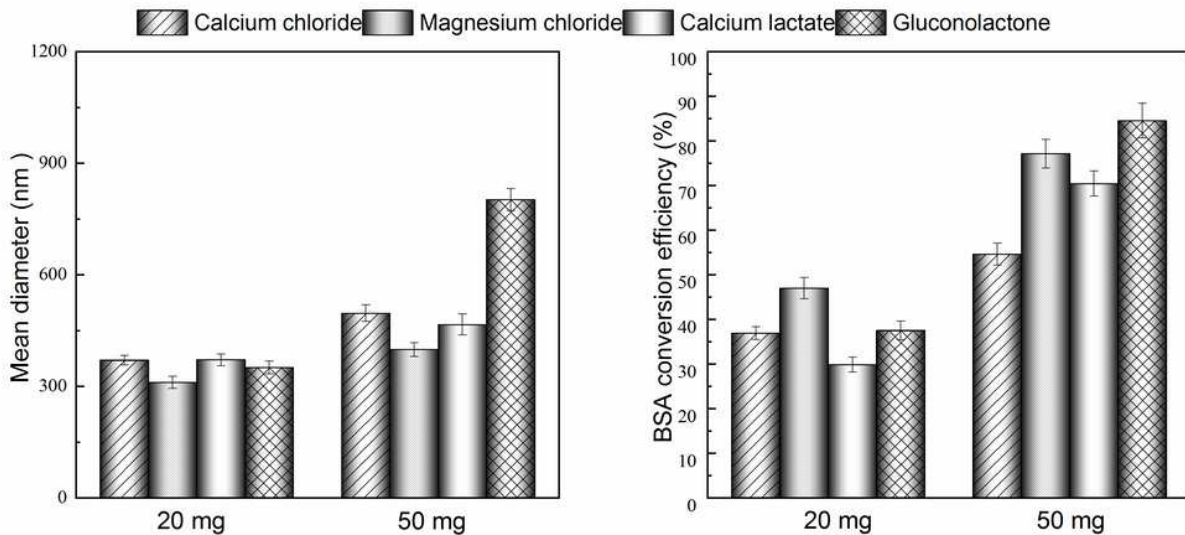


Figure 2

Influence of coagulant concentration and types of coagulants on the mean particle size and BSA conversion efficiency.

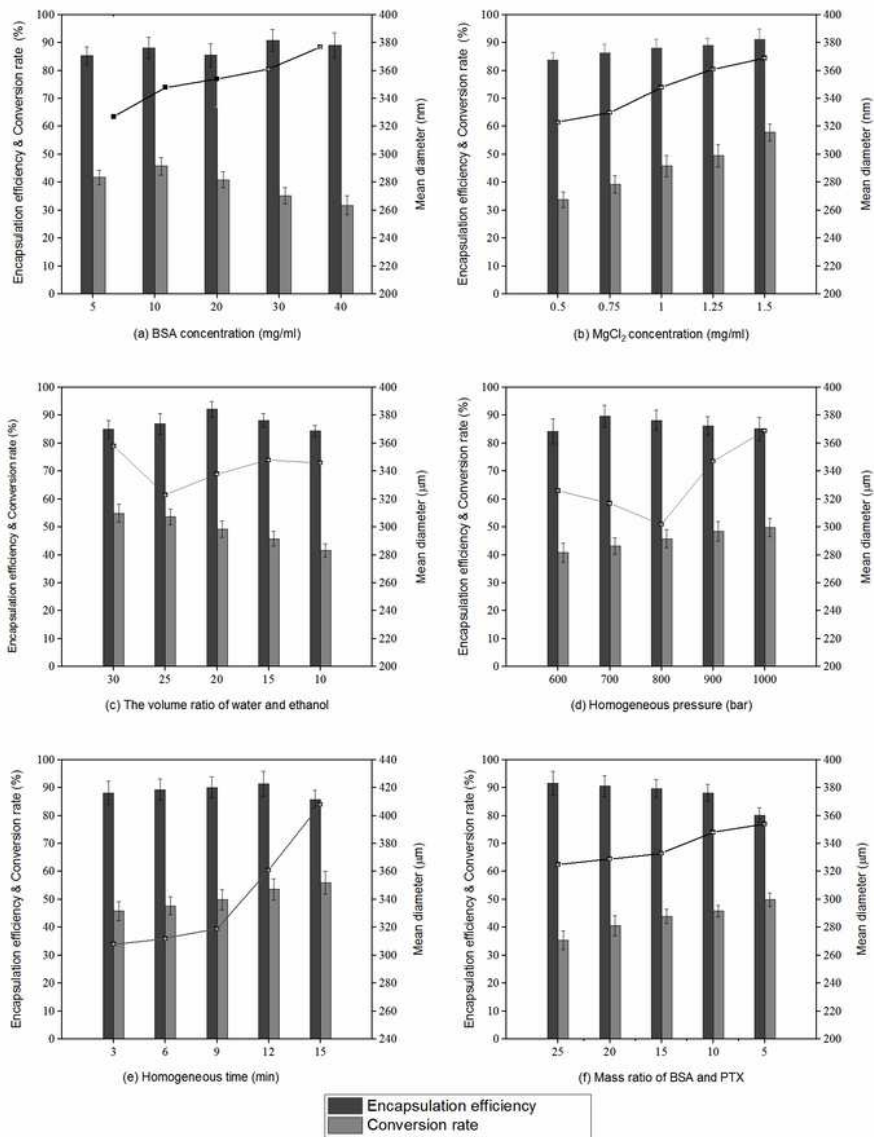


Figure 3

Influence of (a) BSA concentration (mg/mL), (b) MgCl₂ concentration (mg/mL), (c) The volume ratio of water and ethanol, (d) Homogeneous pressure (bar), (e) Homogeneous time (min) and (f) Mass ratio of BSA and PTX on the mean particle size, encapsulation efficiency and total conversion.

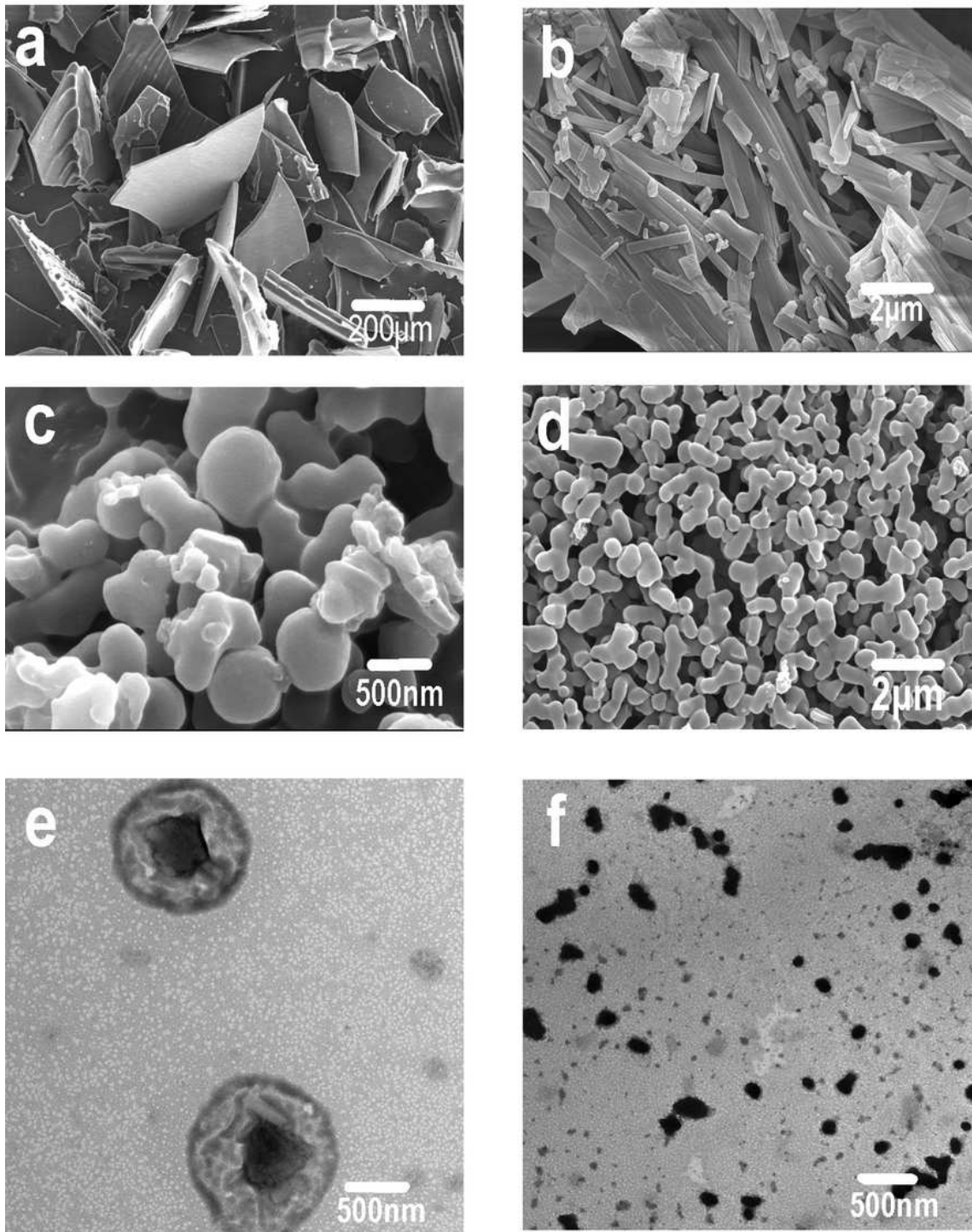


Figure 4

Scanning electron micrographs of BSA(a), PTX(b), BSA-PTX(c) and (d), Transmission Electron Microscopy of BSA-PTX (e) and (f).

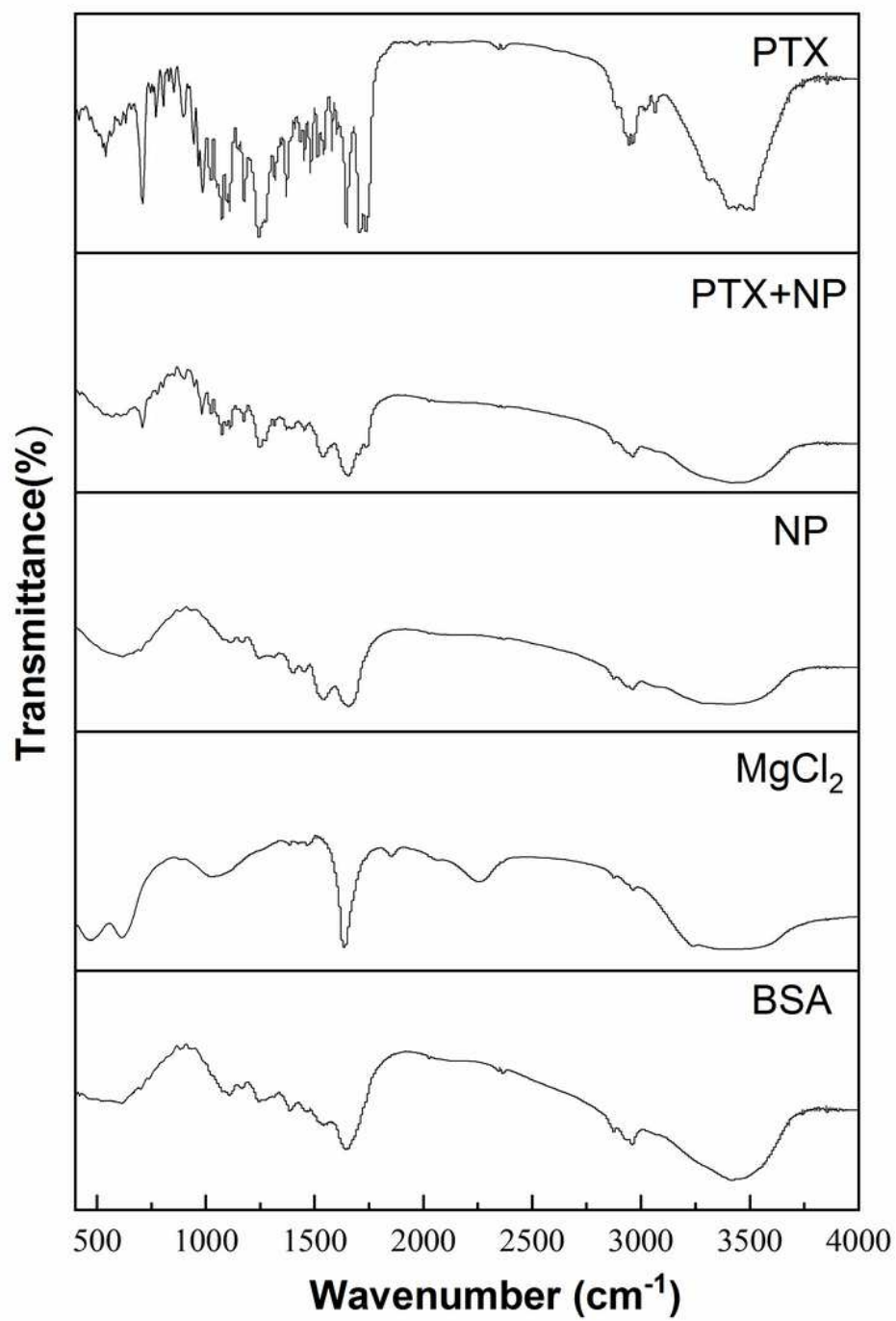


Figure 5

FTIR spectra of BSA; MgCl₂; NP; PTX-BSA; and PTX. The characteristic vibration bands related to BSA and PTX can be seen in the PTX-BSA NPs nanoparticles.

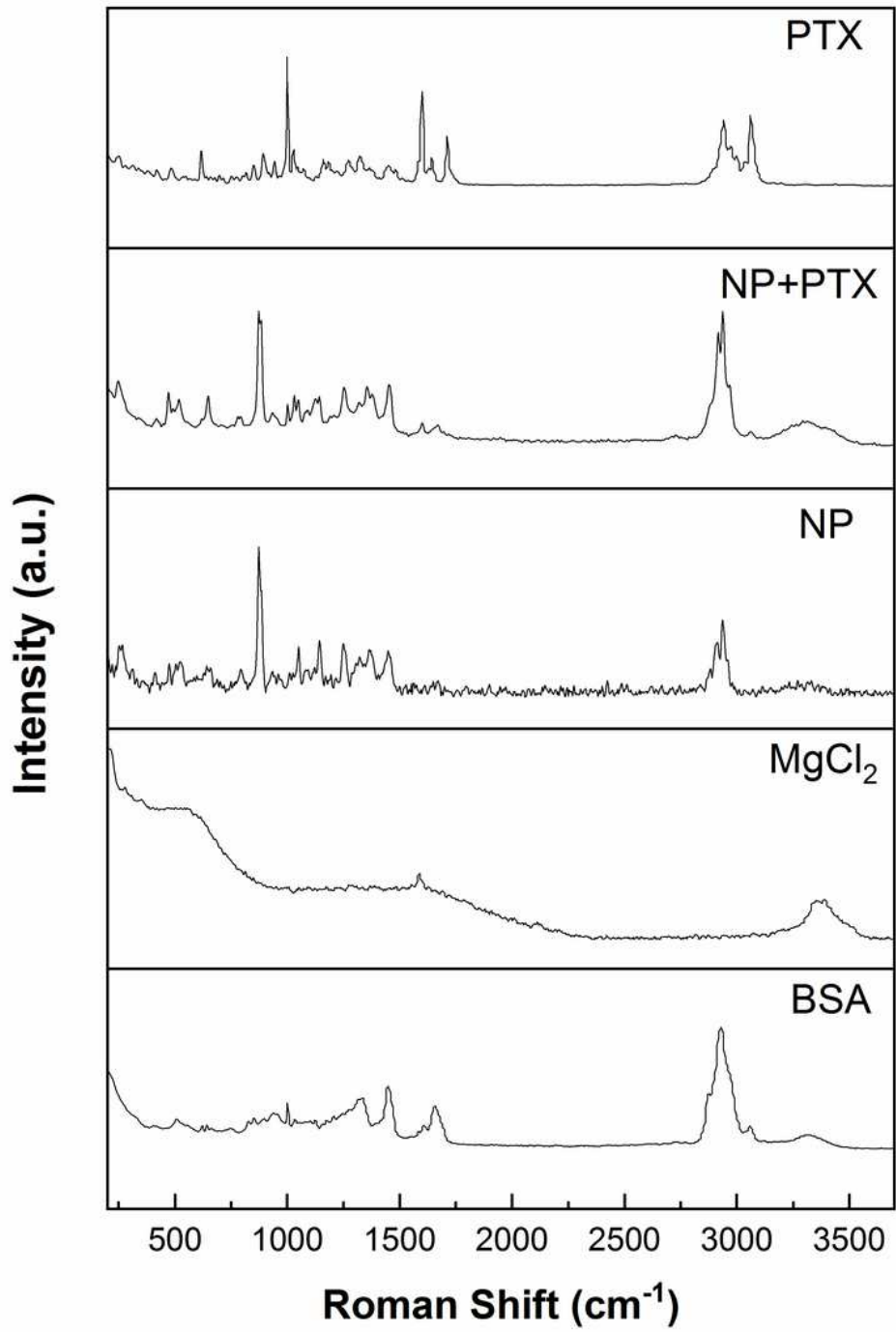


Figure 6

The DSC thermograms of BSA; MgCl₂; NP; PTX-BSA; and PTX .

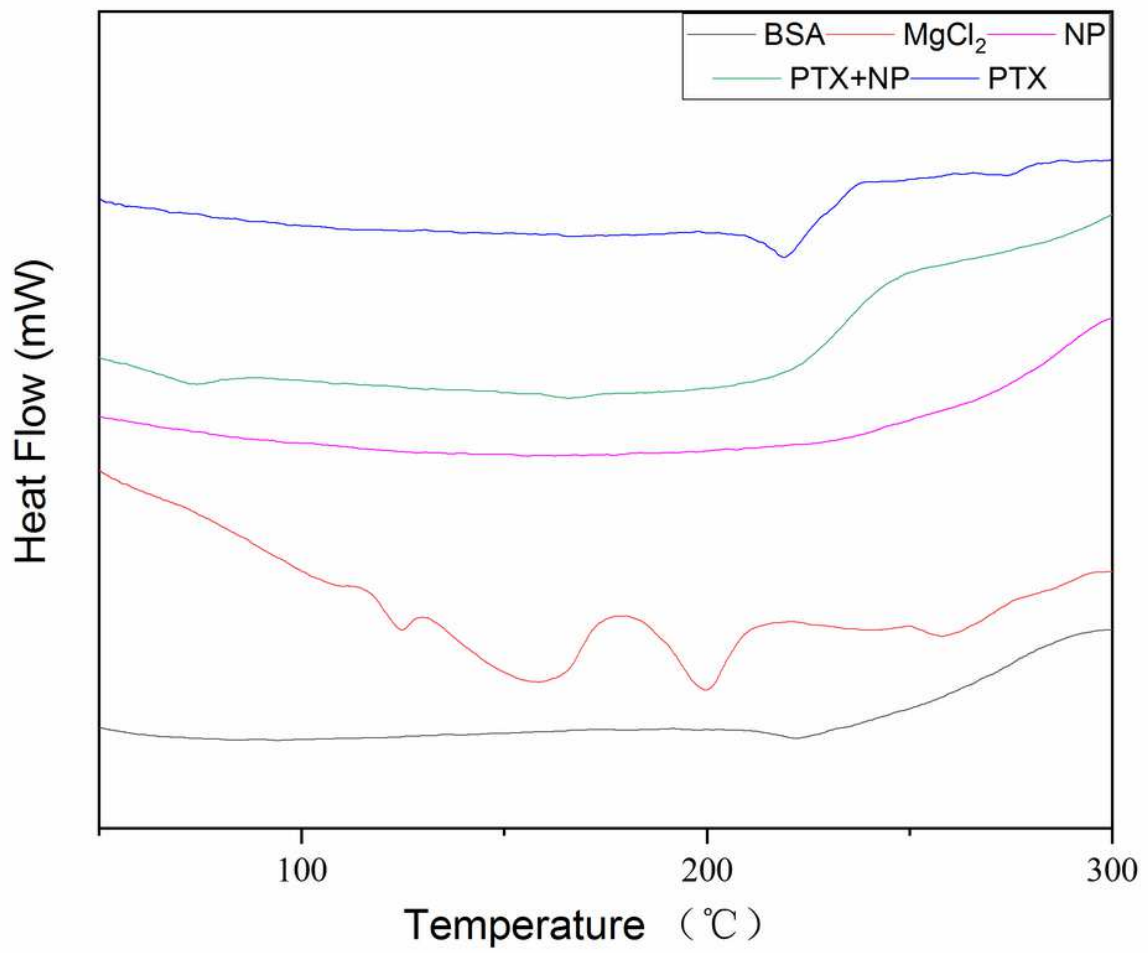


Figure 7

The XRD spectra of BSA ; MgCl₂; NP; PTX-BSA; and PTX .

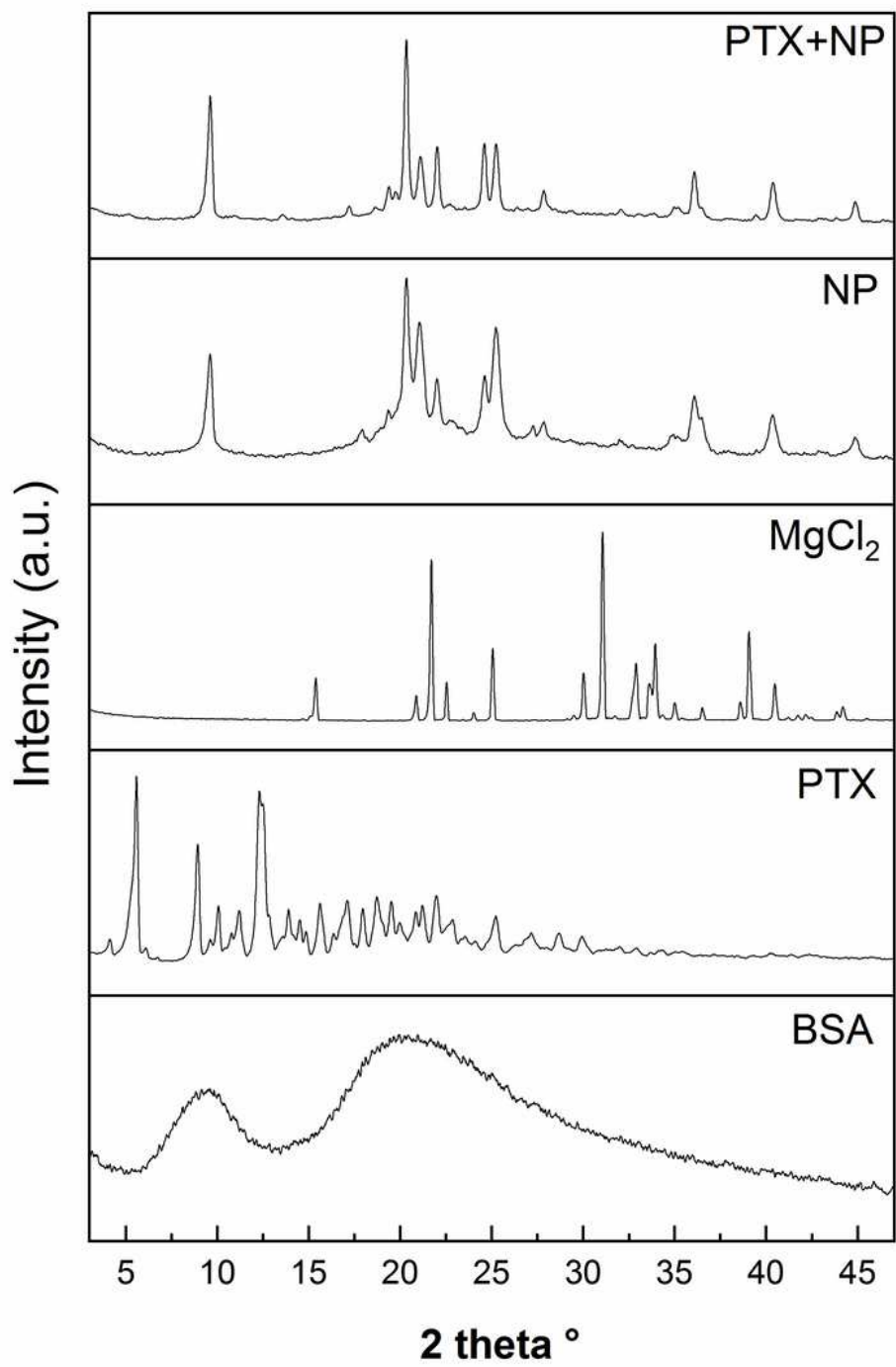


Figure 8

Raman spectrum of BSA; MgCl₂; NP; PTX-BSA; and PTX .

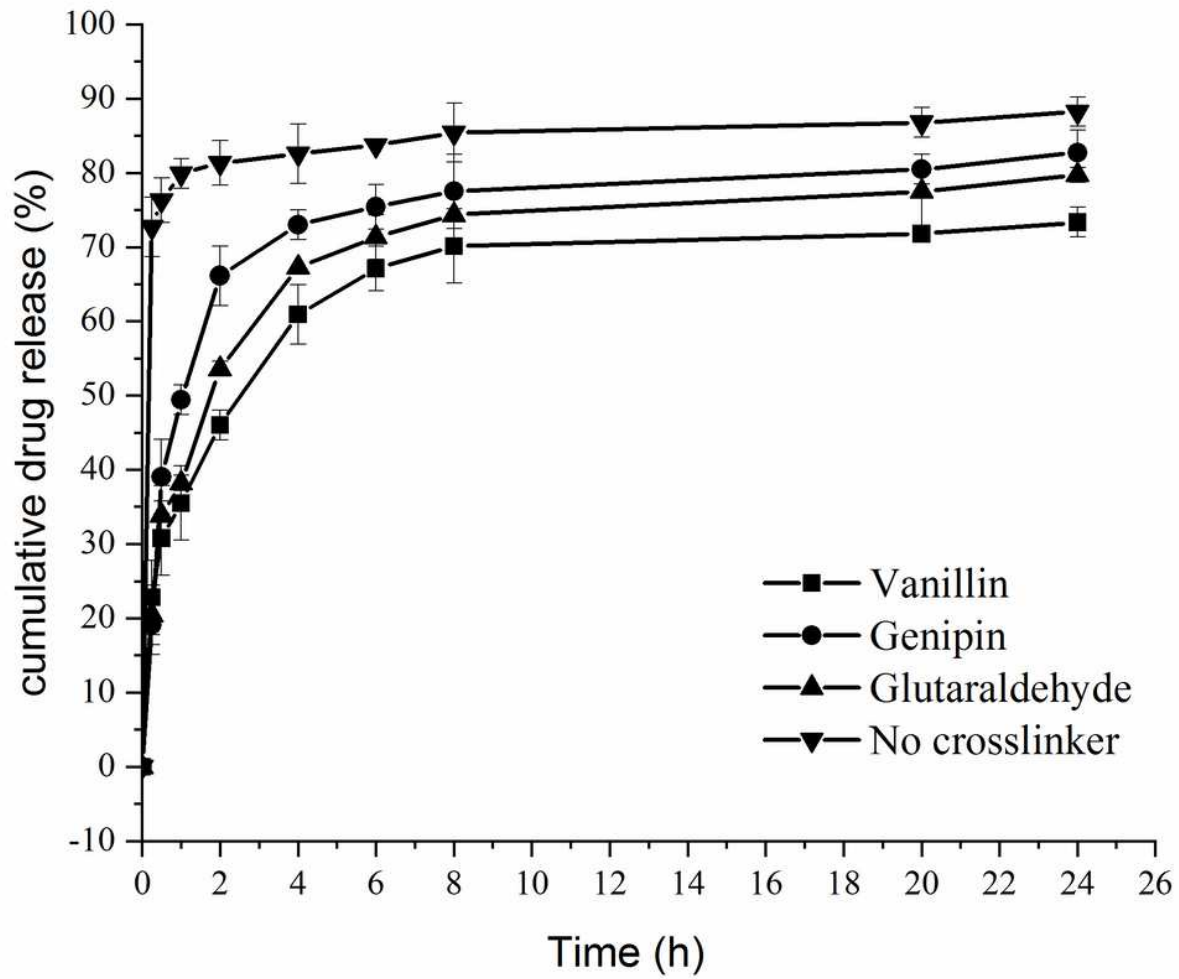


Figure 9

In vitro release profiles of PTX from PTX-BSA. Crosslinking agent dosage, glutaraldehyde/BSA 0.4 μ l/mg; genipin/BSA 0.05 mg/mg; vanillin/BSA 0.02 mg/mg.

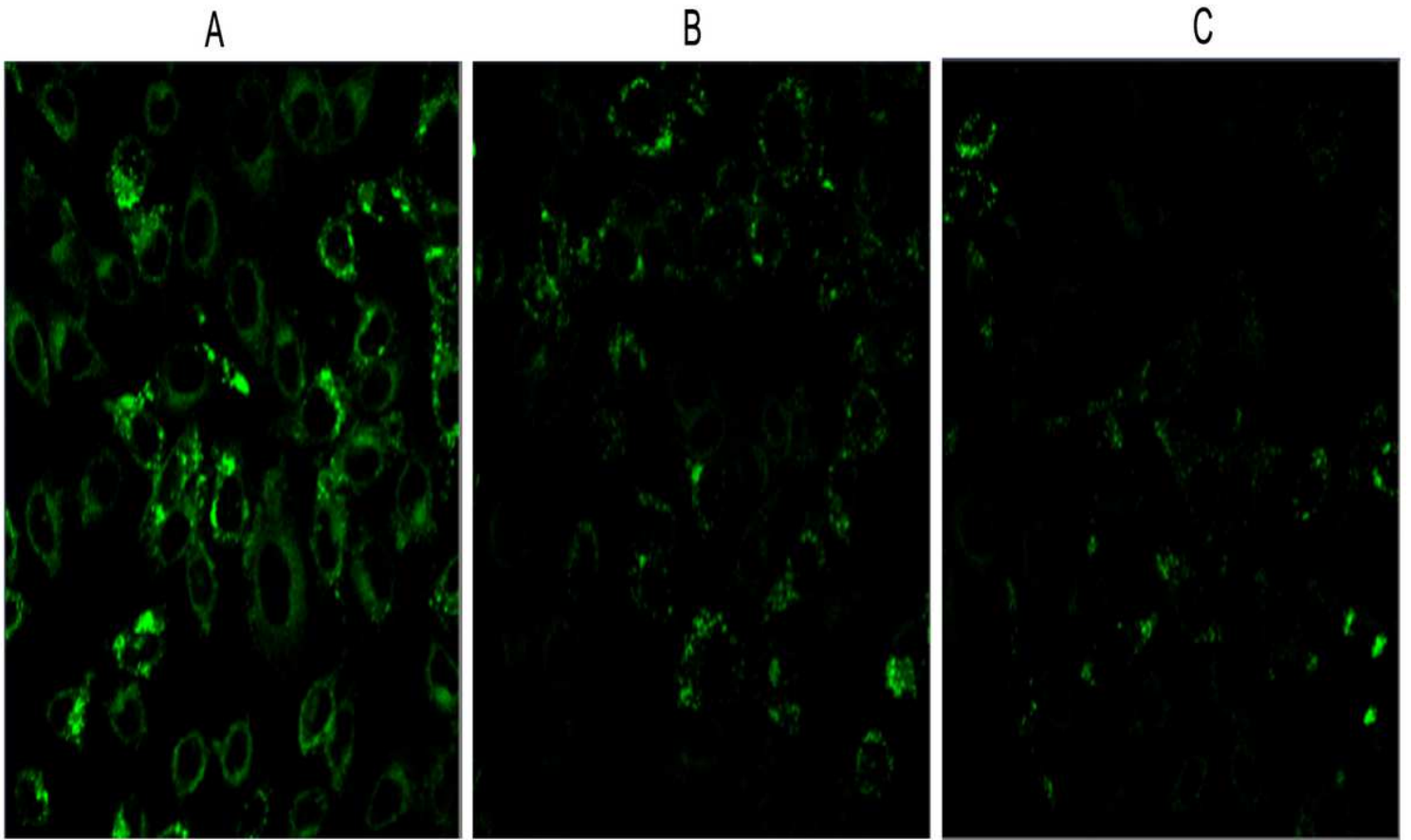


Figure 10

Laser scanning confocal microscope images of HeLa cells after incubation with PTX-BSA. The LSCM images of the FITC-FA-BSA-PTX (A), FITC-BSA-PTX (B) and FITC (C).